Adaptive Droop Control Using Adaptive Virtual Impedance for Microgrids with Variable PV Outputs and Load Demands

Li, Zilin; Chan, Ka Wing; Hu, Jiefeng; Guerrero, Josep M.

Published in:
IEEE Transactions on Industrial Electronics

DOI (link to publication from Publisher):
10.1109/TIE.2020.3022524

Publication date:
2021

Document Version
Accepted author manuscript, peer reviewed version

Adaptive Droop Control Using Adaptive Virtual Impedance for Microgrids with Variable PV Outputs and Load Demands

Zilin Li, Ka Wing Chan, Jiefeng Hu, *Senior Member, IEEE*, Josep M. Guerrero, *Fellow, IEEE*

***Abstract*—In microgrids, intermittency of renewable energy sources (RES) and uncertain state-of-charge (SoC) of energy storage systems (ESS) can cause power deficiency to some distributed generation units (DGs). In this case, DGs with power deficiency may not meet the power demand, resulting in voltage collapse or frequency divergence. Unfortunately, this is seldom considered in inverter control design in existing literature. Thus, in-depth investigation into the microgrid performance under renewable energy resource fluctuations and appropriate control methods are urgently needed. In this paper, an adaptive droop and adaptive virtual impedance control strategy is proposed. Unlike conventional droop control where the droop coefficients are fixed by assuming the DGs can always meet the load demand, the droop coefficients here are adjusted according to actual solar PV power output. In this way, proper power sharing among DGs can be achieved under renewable energy variation. Furthermore, the impact of varying DG capacities on system stability is mathematically investigated. An adaptive virtual impedance is then incorporated into the adaptive droop method to deal with the system instability caused by renewable energy variations. The proposed strategy is analyzed theoretically and validated in MATLAB/Simulink simulation and laboratory experiments. The results demonstrate the advantages of the proposed method over conventional approaches under various scenarios.**

***Key Words*—Adaptive droop, adaptive virtual impedance, instability, large droop gains, microgrid, power deficiency.**

I. Introduction

Microgrids, clusters of distributed generation units (DGs), loads, energy storage systems (ESSs), and the associated power electronic converters, have emerged as an efficient way to facilitate the uptake of renewable energy sources (RES) [1]. A microgrid can work in either grid-tied mode or islanded mode. In the islanded operation, two main control objectives are the reliable power supply and proper load sharing. To achieve these, droop control, which mimics the behavior of a synchronous generator in the power system to increase active and reactive powers by decreasing respectively the frequency and voltage magnitude, is widely utilized to coordinate parallel inverters. The droop coefficients are usually determined by the maximum allowed frequency and voltage deviations and the rated power capacity of each DG. Thus, DGs with larger capacities would have smaller droop coefficients and hence contribute more to load sharing.

In traditional droop control, it is usually assumed that power demanded by the loads can always be supplied by the sources. This may not be true with RES because of intermittency caused by fluctuating wind speed and solar irradiance [2, 3]. This means that the actual capacities of DGs are time-varying, which, unfortunately, is usually ignored by researchers in developing inverter control schemes. If conventional droop approaches with constant droop coefficients are applied, DGs with insufficient capacities may suffer from a power imbalance between generation and load demand, leading to overload and instability issues such as voltage collapse, frequency fluctuation, etc. [4-6]. To achieve a proper load sharing in microgrids facing uncertain available capacities of DGs, various strategies have been proposed, which can be mainly classified into three categories: SoC-balancing strategies [2, 7-9], additional dc voltage droop [4, 10], and adaptive droop control [11, 12].

SoC-balancing strategies are usually aimed to achieve a common SoC to avoid overloading in microgrids with energy storage. Aiming to eliminate the impact of line resistances and to achieve an accurate common SoC, a strategy based on a virtual power concept and communication links is presented in [8]. The strategy is verified under variable generations of RES, communication delays, and different load levels. Nevertheless, communication links inevitably reduce reliability. Inspired by the *P-f* droop control, a SoC-dependent frequency term is added to the original active power droop to obtain a common SoC of distributed ESSs [9]. However, it results in a large frequency deviation. Moreover, the different power capacities of ESSs are not considered. A more practical modified *P-f* droop control in [2] can consider different capacities of distributed ESSs and minimize the frequency deviation simultaneously. The problem is that the ESSs with a relatively low SoC may exhaust their energy before reaching a balanced SoC. Due to the uncertain initial SoC and hardware characteristics of ESSs, the SoC-balancing strategies may take minutes or even hours to reach a common SoC.

On the other hand, RES-powered DGs may not be equipped with ESSs for cost reduction. Without the energy buffer, the available power of the DGs will heavily depend on weather conditions. Therefore, they are more likely to experience power imbalance issues. In [10], to avoid dc voltage collapses during variations of sunlight or load transients, a PID controller is designed to reduce the droop frequency according to the error between the PV dc voltage and the reference. Similarly, an enhanced dual droop control in [4] can also cope with the power deficiency issue. However, the droop gains in [4] and [10] are kept constant, which limits the control flexibility of the droop controller to tackle RES uncertainties. In this regard, adaptive

droop control is developed in [11, 12] to continuously adjust the droop coefficients in reciprocal to the available power of the source, such that the output powers will be kept proportional to their actual available capacities and overload scenarios are avoided. Nevertheless, references [11] and [12] shows following limitations.

- The adaptive droop coefficients may experience large variations due to the intermittency of RES. Large droop coefficients can make a microgrid system prone to low-frequency instability.
- How exactly the adaptive droop coefficients impact the DG output impedance and hence, the stability of the whole microgrid, is still not revealed mathematically.

To address the instability, actually some efforts have been paid by researchers. For example, in [5] the impact of fuzzy-logic-based adaptive droop coefficients on the system stability is analyzed via eigenvalues. A full-order microgrid model is developed to identify the oscillatory mode caused by droop coefficients [13]. The influence of droop coefficients on microgrid with complex line impedance can be also found in [14], [15]. However, these strategies are not discussed to minimize the reverse impact of droop coefficients.

Recently, virtual impedance concept has been introduced to improve system performance, such as active stabilization [16-19], accurate reactive power sharing [20, 21], unbalanced and harmonic load sharing [18, 20-24]. Nevertheless, virtual impedance scheme has seldom been utilized to improve system stability. The main challenge is to design a proper size of the virtual impedance. In [25], a detailed small-signal model of the whole system is utilized to define the feasible and optimal range for the virtual impedance. This method can be problematic in microgrids consisting of a large number of DGs and reconfigurable network topologies. Additionally, physical insight cannot be revealed by the state-space model. Recently, a Lyapunov-based droop stability certificate is presented for designing virtual impedance [26], which can achieve a concise and simple association of droop coefficients and the desired virtual impedance. Although a stable system can be ensured, the method treats the coefficients of the active and reactive droop equally, and the droop stability is highly sensitive to the active droop coefficient.

To date, to the best of our knowledge, existing research still lacks a mathematical method to determine the proper size of the virtual impedance to ensure stability by considering solar PV output variations and adaptive droop coefficients. This motivates us to develop a new adaptive droop and adaptive virtual impedance control strategy to address this practical and important problem. Specifically, the adaptive droop is to handle varying DGs power outputs, while the adaptive virtual impedance is to deal with the droop instability. The main contributions can be highlighted as follows:

1) The shaping effect of varying droop coefficients on the DG output impedance is analyzed thoroughly and the droop instability is revealed using impedance-based method.

2) An analytical method is proposed to determine the size of the adaptive virtual impedance to ensure system stability by considering renewable energy fluctuations, droop controller parameters, and inherent output impedance.

3) The adaptive droop and adaptive virtual impedance control strategy enables a microgrid operating safely under wide variations of available power of DGs. Comparisons with existing methods are conducted to demonstrate the advantages of the proposed method.

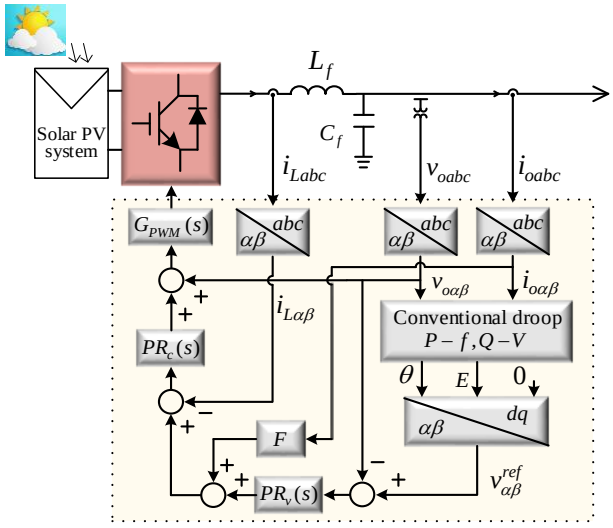

Fig. 1 Single-line diagram of a droop controlled DG in three-phase Microgrids

II. Shortcomings of Traditional Droop Control

In existing research, it is usually assumed that DGs can always deliver as much power as demanded by loads. This assumption may be true for DGs using conventional fossil fuel in a well-scheduled system because the fuel is usually prepared beforehand. However, in a microgrid where the loads are supplied by RES, the available power of DGs is significantly influenced by weather conditions. Therefore, available capacities of DGs can change and are likely less than the rated value. Fig. 1 illustrates the *P-f* and *Q-V* droop for load sharing among distributed inverters in AC microgrids. Conventionally, the droop coefficients can be expressed as

$$m = \Delta\omega / S_N \,, n = \Delta V / S_N \tag{1}$$

where $\Delta\omega$ and ΔV are the maximum allowed deviations of angular frequency and voltage amplitude, respectively. S_N is the DG rated capacity. After the voltage references are generated by the droop controller in Fig. 1, a dual-loop voltage and current control using proportional and resonant controllers are utilized to produce PWM signals to control the inverter.

Now the problem is that, if constant coefficients are used corresponding to a constant rated DG capacity, as depicted in (1), the load demand may exceed the DG's actual capacity when the RES output fluctuates. As a result, a stable system frequency and the voltage of the DG cannot be retained. To address this problem, droop coefficients should be adjusted accordingly to the available capacity of a DG as [11, 12]

$$m = \Delta\omega / S_a \,, n = \Delta V / S_a \tag{2}$$

where S_a is the available power capacity. By using adaptive droop coefficients, proper power-sharing among DGs can be

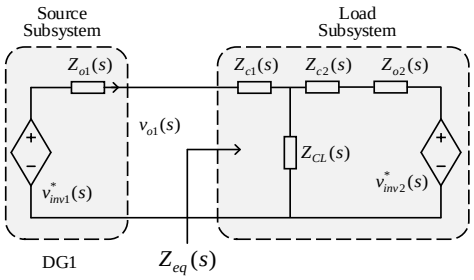

Fig. 2 Source- and load-subsystems of the microgrid system

achieved even DGs' capacities vary.

III. Impact of Droop Coefficients on System Stability under Renewable Energy Fluctuation

Even although the adaptive droop coefficients in (2) can enable proper load sharing among DGs according to their actual capacities, they may experience large variations due to the fluctuation outputs of RESs. The variations of droop coefficients could have a great impact on characteristics of the DG output impedance and hence, the stability of the whole microgrid.

A. Output impedance model of droop-controlled inverters

To illustrate how the droop coefficients cause instability issues, a small-signal output impedance model of the DG in Fig. 1 is developed here using the harmonic linearization method [27]. The output voltage and current of the DG with perturbated signals can be expressed under the stationary frame as

$$\begin{cases} v_{o\alpha} = V_1\cos 2\pi f_1 t + V_p\cos(2\pi f_p t+\varphi_{vp}) \\ v_{o\beta} = V_1\sin 2\pi f_1 t + V_p\sin(2\pi f_p t+\varphi_{vp}) \\ i_{o\alpha} = I_1\cos(2\pi f_1 t+\varphi_{c1}) + I_p\cos(2\pi f_p t+\varphi_{cp}) \\ i_{o\beta} = I_1\sin(2\pi f_1 t+\varphi_{c1}) + I_p\sin(2\pi f_p t+\varphi_{cp}) \end{cases} \tag{3}$$

where V_1 and I_1 are magnitudes of the voltage and current at the fundamental frequency f_1. φ_{c1} is the initial phase angle relative to the voltage at f_1. V_p and φ_{vp} are the magnitude and phase angle of the perturbated voltage signal at f_p, and the corresponding current magnitude and phase angle are I_p and φ_{cp}, respectively. The output powers can be calculated in the droop controller as

$$\begin{cases} p = \frac{3}{2}\left(v_{o\alpha}i_{o\alpha} + v_{o\beta}i_{o\beta}\right) \\ q = \frac{3}{2}\left(-v_{o\alpha}i_{o\beta} + v_{o\beta}i_{o\alpha}\right) \end{cases} \tag{4}$$

here p and q are the instantaneous active and reactive power respectively. A low-pass filter (LPF) is required to get averaged power signals and to decouple the droop and the inner voltage controller

$$LPF(s) = \omega_c \big/ s+\omega_c \tag{5}$$

where ω_c is the cutoff frequency. Then, the averaged power signals of a DG can be calculated in the frequency domain as

$$P[f] = \begin{cases} \frac{3}{2}V_1I_1\cos\varphi_{c1}\cdot LPF(s)G_s^2(s) & ,\text{dc} \\ \frac{3}{4}LPF(s)G_s^2(s)\left[V_1I_pe^{\pm j\varphi_{cp}} + V_pI_1e^{\pm j(\varphi_{vp}-\varphi_{c1})}\right] & ,f=\pm(f_p-f_1) \end{cases}$$
$$Q[f] = \begin{cases} -\frac{3}{2}V_1I_1\sin\varphi_{c1}\cdot LPF(s)G_s^2(s) & ,\text{dc} \\ -\frac{3}{4}LPF(s)G_s^2(s)\left[V_1I_pe^{\pm j\left(\varphi_{cp}-\frac{\pi}{2}\right)} - V_pI_1e^{\pm j\left(\varphi_{vp}-\varphi_{c1}-\frac{\pi}{2}\right)}\right] & ,f=\pm(f_p-f_1) \end{cases} \tag{6}$$

where $G_s(s)$ is the signal sampling effect. The power terms with second-order perturbated signals are neglected. As shown in (6), the dc components in P and Q are associated with the fundamental voltage and current, while the ac components at $\pm(f_p$-$f_1)$ are generated by the fundamental and perturbated voltages and currents together. Since the conventional P-f and Q-V droop control is adopted in this paper, the synchronous phase and voltage magnitude are expressed as

$$\theta = \frac{1}{s}\left[\omega_0 - m\cdot P\right], E = E_0 - n\cdot Q \tag{7}$$

The active and reactive power signals will change the outputs from the droop controller, which can be defined as

$$\theta = \theta_1 + \Delta\theta, E = E_1 + \Delta E \tag{8}$$

where θ_1 and E_1 are steady-state values. $\Delta\theta$ and ΔE are the perturbated values. Substituting (6) into (7) yields

$$\theta[f] = \begin{cases} \frac{1}{s}\left[\omega_0 - \frac{3}{2}mV_1I_1\cos\varphi_{c1}LPF(s)G_s^2(s)\right] & ,dc \\ -\frac{3}{4}\frac{mLPF(s)G_s^2(s)}{s}\left[V_1I_pe^{\pm j\varphi_{cp}} + V_pI_1e^{\pm j(\varphi_{vp}-\varphi_{c1})}\right] & ,f=\pm(f_p-f_1) \end{cases}$$
$$E[f] = \begin{cases} E_0 + \frac{3}{2}nV_1I_1\sin\varphi_{c1}LPF(s)G_s^2(s) & ,dc \\ \frac{3}{4}nLPF(s)G_s^2(s)\left[V_1I_pe^{\pm j\left(\varphi_{cp}-\frac{\pi}{2}\right)} - V_pI_1e^{\pm j\left(\varphi_{vp}-\varphi_{c1}-\frac{\pi}{2}\right)}\right], & f=\pm(f_p-f_1) \end{cases} \tag{9}$$

As shown in (9), θ_1 and E_1 are corresponding to the dc components; $\Delta\theta$ and ΔE are caused by the perturbations in the power signals and can be expressed in the frequency domain as

$$\Delta\theta[f] = -\frac{3}{4}\frac{mLPF(s)G_s^2(s)}{s}\left[V_1I_pe^{\pm j\varphi_{cp}} + V_pI_1e^{\pm j(\varphi_{vp}-\varphi_{c1})}\right] \quad ,f=\pm(f_p-f_1)$$
$$\Delta E[f] = \frac{3}{4}nLPF(s)G_s^2(s)\left[V_1I_pe^{\pm j\left(\varphi_{cp}-\frac{\pi}{2}\right)} - V_pI_1e^{\pm j\left(\varphi_{vp}-\varphi_{c1}-\frac{\pi}{2}\right)}\right], f=\pm(f_p-f_1) \tag{10}$$

The voltage references from the droop controller are

$$\begin{cases} v_\alpha^{ref}(t) = E\cdot\cos\theta \\ v_\beta^{ref}(t) = E\cdot\sin\theta \end{cases} \tag{11}$$

The three-phase system is assumed to be balanced, so it is sufficient to consider the terms on α axis. Substituting (8) into (11), and neglecting the second-order terms, the variation of the voltage reference on α-axis can be obtained as

$$\Delta\mathbf{V}_\alpha^{ref}[f] = \cos\theta_1[f] * \Delta E[f] - E_1\sin\theta_1[f] * \Delta\theta[f] \tag{12}$$

where $*$ denotes convolution. The cosine and sine functions are

$$\cos\theta_1[f] = \frac{1}{2}e^{\pm j\sigma_0}, \sin\theta_1[f] = \frac{1}{2}e^{\pm j\left(\sigma_0-\frac{\pi}{2}\right)}, f=\pm f_1 \tag{13}$$

where σ_0 is the phase angle between θ_1 and the reference. Then, substituting (10) and (13) into (12), and neglecting terms with frequency $\pm(f_p-2f_1)$, the variation can be expressed as

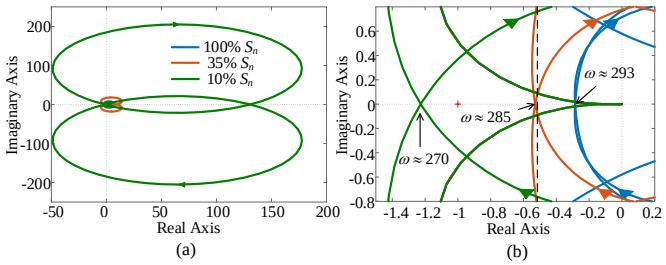

Fig. 3 Nyquist diagrams of the impedance ratio when S_a of DG1 is 100%, 35% and 10% of rating, respectively. (a) Full view. (b) Zoom-in view

$$\Delta \mathbf{V}_{\alpha}^{ref}[f]=\frac{3}{8}LPF(s\mp j2\pi f_1)G_s^2(s\mp j2\pi f_1)e^{\pm j\left(\sigma_0-\frac{\pi}{2}\right)}\left[n+\frac{mE_1}{s\mp j2\pi f_1}\right]\cdot V_1 I_p e^{\pm j\varphi_{vp}}$$
$$+\frac{3}{8}LPF(s\mp j2\pi f_1)G_s^2(s\mp j2\pi f_1)e^{\pm j\left(\sigma_0-\frac{\pi}{2}\right)}\left[-n+\frac{mE_1}{s\mp j2\pi f_1}\right]\cdot V_p I_1 e^{\pm j(\varphi_{vp}-\varphi_{c1})},\ f=\pm f_p \quad (14)$$

After the voltage references are generated by the droop controller, they are fed into the inner dual-loop controller. The inverter output voltage can be expressed by transfer functions

$$v_{o\alpha}(s)=G_v(s)\cdot v_{\alpha}^{ref}(s)-G_c(s)\cdot i_{o\alpha}(s) \quad (15)$$

where $G_v(s)$ and $G_c(s)$ are the closed-loop transfer functions from voltage reference and output current to the output voltage, respectively. The output impedance of the inverter is defined as the ratio of $\Delta \mathbf{V}_{o\alpha}[f]$ and $-\Delta \mathbf{I}_{o\alpha}[f]$, and

$$\Delta \mathbf{V}_{o\alpha}[f]=\frac{V_p}{2}e^{\pm j\varphi_{vp}},\Delta \mathbf{I}_{o\alpha}[f]=\frac{I_p}{2}e^{\pm j\varphi_{cp}},\ f=\pm f_p \quad (16)$$

Substitute (14) and (16) into (15), the output impedance can be obtained

$$Z_o(s)=\frac{G_c(s)-\frac{3}{4}V_1 e^{j\left(\sigma_0-\frac{\pi}{2}\right)}G_v(s)LPF(s-j2\pi f_1)G_s^2(s-j2\pi f_1)(n+\frac{mE_1}{s-j2\pi f_1})}{1+\frac{3}{4}I_1 e^{j\left(\sigma_0-\varphi_{c1}-\frac{\pi}{2}\right)}G_v(s)LPF(s-j2\pi f_1)G_s^2(s-j2\pi f_1)(n-\frac{mE_1}{s-j2\pi f_1})} \quad (17)$$

B. Impact of droop coefficients on the system stability

As shown in (17), the droop coefficients can modify the output impedance of a DG, which has not been studied in the literature [28-30]. To investigate the influence of the droop coefficients, DGs are represented in their Thevenin circuits with the output impedance model in (17). Fig. 2 shows a two-DG system and the parameters are shown in Table III. For easy illustration, the droop coefficients in DG1 are varied while those of DG2 are kept constant. The equivalent impedance of the load-subsystem can be calculated as

$$Z_{eq}=Z_{c1}+\left(Z_{c2}+Z_{o2}\right)\|Z_{CL} \quad (18)$$

where Z_{c1} and Z_{c2} are connecting impedances, Z_{CL} the common load, and Z_{o2} the output impedance of the DG2. Then according to the impedance-based method, the impedance ratio is

$$G_R=Z_{o1}/Z_{eq} \quad (19)$$

According to the Nyquist stability criterion, a system is stable if the number of poles of G_R on the right-half s plane, P, is equal to the number of counterclockwise encirclement of (-1,0), N, i.e., P=N. For three different available capacities (100%, 35%, 10%) of DG1 resulting in three sets of different droop coefficients, the Nyquist diagrams of G_R are plotted in Fig. 3. The pole-zero maps of G_R show that P=0 for the capacities, which are not presented here due to limited space. As illustrated in Fig.3, the Nyquist curves change when the droop coefficients vary. The zoom-in view in Fig. 3(b) reveals that when S_a decreases, i.e., the droop coefficients increase, the crossover point approaches the critical point (-1,0), indicating a reduced stability margin. Specifically, if S_a is only 10% of the rated value, the critical point (-1,0) will be encircled clockwise twice with N=−2, resulting in P $\neq$ N, and thus indicating an unstable system.

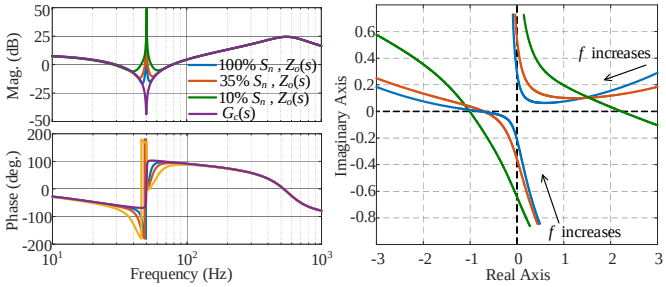

Fig. 4 (a) Bode diagram of the output impedance $Z_o(s)$ with different droop coefficients and the inherent impedance $G_c(s)$; (b) Zoom-in view of Real- and Imaginary-part of $Z_o(s)$ in the frequency range from 30Hz to 70Hz.

IV. PROPOSED ADAPTIVE DROOP AND ADAPTIVE VIRTUAL IMPEDANCE CONTROL STRATEGY

From the previous analysis in Section III, it has been revealed that the adaptive droop coefficients due to the fluctuations of renewable energy can influence significantly the characteristics of the DG output impedance and subsequently the whole system stability. As shown in Fig. 4(a), by observing frequency responses of $Z_o(s)$ and $G_c(s)$, one can conclude that the droop control has a great effect on both magnitude and phase of the output impedance around the operating frequency. Thus, using only $G_c(s)$ may not achieve a satisfactory result for low-frequency stability analysis. Varying droop coefficients can change the shape of $Z_o(s)$ notably, as presented in Fig. 4(a). The real and imaginary parts of $Z_o(s)$ in Fig. 4(b) can illustrate more clearly the shaping effect. Specifically, large droop coefficients will result in smaller negative real parts at subsynchronous frequencies, which are the root cause of droop instability. Virtual impedance can be adopted to minimize the negative real parts and to enhance system stability. However, the key is the proper design of the virtual impedance.

For generality, the inner-loop controllers have been designed in the per-unit form. When a series virtual impedance $Z_{v,pu}(s)$ is introduced, the output impedance in (17) becomes

TABLE I CALCULATED VIRTUAL RESISTANCE BY (22) AT 47Hz

S_a%	100%	90%	80%	70%	60%	50%	40%	30%	25%	20%	15%	10%	8%	5%
$R_{v,pu}$	0.0254	0.0286	0.0336	0.0399	0.0485	0.0605	0.0784	0.1084	0.1325	0.1681	0.2283	0.3483	0.4376	0.708

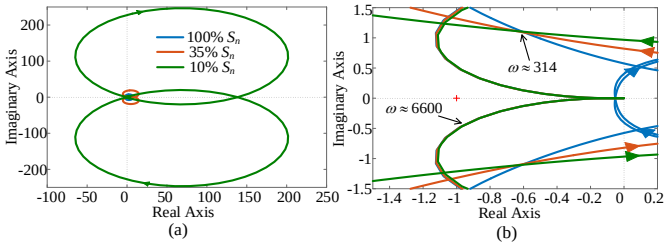

Fig. 5 With the designed virtual impedance, Nyquist diagrams of the impedance ratio when S_a of DG1 is 100%, 35% and 10% of the rated value, respectively. (a) Full view. (b) Zoom-in view

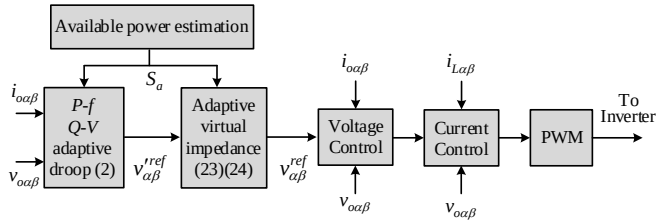

Fig. 6 Block diagram of the overall control strategy

$$Z_o(s)=\frac{Z_{base}G_{c,pu}(s)+Z_{base}Z_{v,pu}(s)-\frac{3}{4}\frac{S_N}{S_a}\frac{V_1E_1}{S_N}e^{j\left(\sigma_0-\frac{\pi}{2}\right)}LPF(s-j2\pi f_1)\left(\frac{\Delta V}{E_1}+\frac{\Delta\omega}{s-j2\pi f_1}\right)}{1+\frac{3}{4}\frac{I_1E_1}{S_a}e^{j\left(\sigma_0-\varphi_{c1}-\frac{\pi}{2}\right)}LPF(s-j2\pi f_1)\left(\frac{\Delta V}{E_1}-\frac{\Delta\omega}{s-j2\pi f_1}\right)} \quad (20)$$

where $G_{c,pu}(s)$ is the inherent output impedance due to the inner-loop control, Z_{base} is impedance base. $G_v(s)$ and the signal sampling effect $G_s(s\text{-}j2\pi f_1)$ have been ignored due to their negligible effect on $Z_o(s)$ at the subsynchronous frequencies. According to (20), $Z_{v,pu}(s)$ can only influence the numerator of $Z_o(s)$. For design convenience, it is also reasonable to assume that $V_1\approx E_1\approx E_0$ and $\sigma_0\approx 0$, where E_0 is the rated voltage magnitude. Then, for an ideal voltage source, the numerator of $Z_o(s)$ should be zero, therefore $Z_{v,pu}(s)$ should be

$$Z_{v,pu}(s)=\frac{-jS_N}{2S_a}LPF(s-j2\pi f_1)\left(\frac{\Delta V}{E_0}+\frac{\Delta\omega}{s-j2\pi f_1}\right)-G_{c,pu}(s) \quad (21)$$

Yet, it is impractical to achieve a zero value at all frequencies due to the high nonlinearity in (21). Instead, $Z_{v,pu}(s)$ is designed to reduce the subsynchronous frequency range having negative real parts, which is realized by the virtual resistance $R_{v,pu}$ of $Z_{v,pu}(s)$. Now, the key becomes how to select the value of $R_{v,pu}$ under varying available capacities. As explained in the stability analysis in Section III, the instable subsynchronous frequencies mainly fall into the range of 42~47Hz, and the closer the frequency to the nominal, the smaller the negative real part, as illustrated in Fig. 4. Therefore, the frequency 47Hz will be selected to calculate the virtual impedance, then

$$R_{v,pu}\left(\frac{S_N}{S_a}\right)=\mathrm{Re}\left[\frac{-jS_N}{2S_a}LPF\left[j2\pi(47-f_1)\right]\left(\frac{\Delta V}{E_0}+\frac{\Delta\omega}{j2\pi(47-f_1)}\right)-G_{c,pu}\left[j2\pi(47-f_1)\right]\right] \quad (22)$$

In a specific system, $\triangle V$, $\triangle\omega$, and E_0 are identical for all DGs. Thus, using the parameters in Table II, the required per-unit virtual resistance can be calculated with different S_a by (22), as shown in Table I. With the help of the curve fitting tool in MATLAB, the virtual resistance can be formulated as

$$R_{v,pu}\left(\frac{S_N}{S_a}\right)=0.036\frac{S_N}{S_a}-0.0115 \quad (23)$$

Inductive reactance is also incorporated with $R_{v,pu}/X_{v,pu}$=1, then the virtual impedance can be expressed as

$$Z_{v,pu}(s)=R_{v,pu}\cdot(1+j1)\cdot\frac{1}{sT_v+1} \quad (24)$$

A low-pass filter with T_v=0.001s is utilized to reduce the influence of the virtual impedance on the high-frequency range. As shown in Fig. 5, after compensation with the designed virtual impedance, the Nyqsuit curves of (19) do not encircle the critical point (-1, 0) anymore when S_a is 100%, 35%, and 10%, demonstrating the effectiveness of the adaptive virtual impedance. For better illustration, the overall proposed adaptive virtual impedance droop control strategy is depicted in Fig. 6.

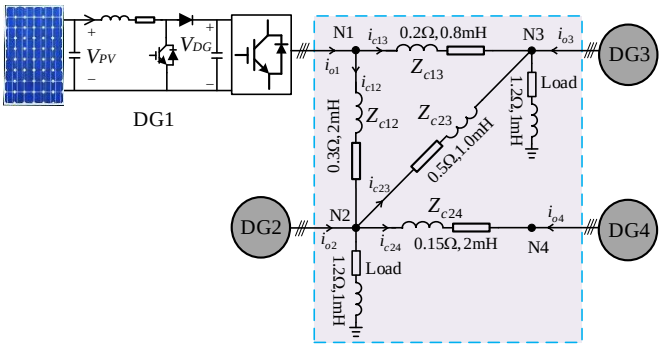

Fig. 7 Single-line diagram of the three-phase three-wire AC microgrid in Simulation

TABLE II RATED POWER OF DGS AND OTHER PARAMETERS IN SIMULATION

Symbol	Description	Values
S_{n1}/ S_{n2}	Rated power of DG1 and DG2	10/30kVA
S_{n3}/ S_{n4}	Rated power of DG3 and DG4	40/20kVA
E_0	Rated voltage magnitude	165V
ω_0	Rated angular frequency	314.159rad/s
f_s	Switching frequency	21kHz
V_{dc}	DC voltage	450V
$\triangle\omega$	Allowed frequency deviation	0.004 p.u.
$\triangle V$	Allowed voltage deviation	0.05 p.u.
ω_c	Cutoff frequency of LPF	30rad/s
L_f	Filter inductance	0.2308 p.u.
C_f	Filter capacitance	0.0513 p.u.
k_{pv}	Proportional gain of voltage controller	0.817
k_{iv}	Resonant gain of voltage controller	265
k_{pc}	Proportional gain of current controller	1.96
F	Feedforward gain of output current	0.6
T_{ss}	Time constant of LPF in sampling	0.00015s

V. SIMULATION RESULTS

To verify the proposed control strategy, a three-phase three-wire microgrid in Fig. 7 is simulated in MATLAB/Simulink. The system parameters are listed in Table II. DG1 is powered by a 10kW PV panel with a boost converter. The available power of DG1 varies according to the solar irradiance, based on which the droop coefficients are altered. The other three DGs are powered by dc voltage sources with their rated powers. The

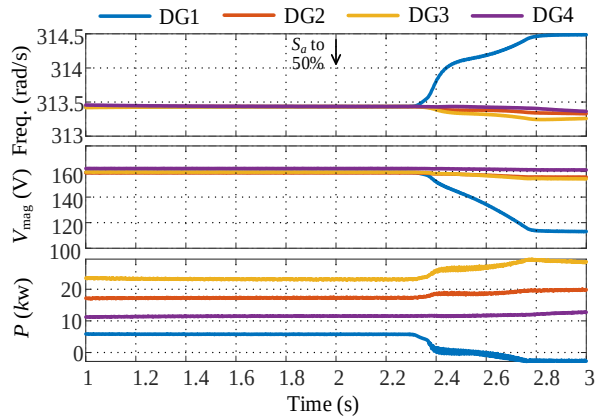

Fig. 8 Simulation results with fixed droop coefficients and $Z_{v,pu}$=0.036+j0.036

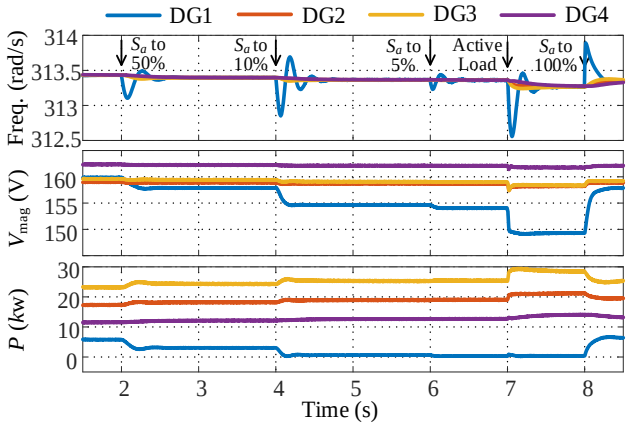

Fig. 10 Simulation results with adaptive droop and virtual impedance designed by the plug-and-play rule in [26]

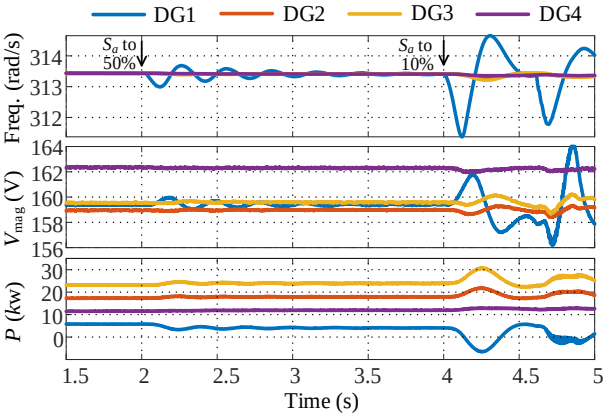

Fig. 9 Simulation results with enhanced dual-droop strategy in [4]

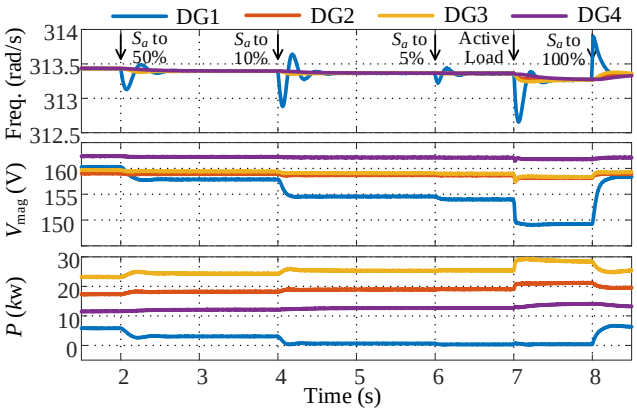

Fig. 11 Simulation results with the proposed adaptive droop and adaptive virtual impedance control

loads connected at nodes N2 and N3 are Z=1.2+j0.314Ω. In the beginning, S_a of DG1 is the rated value and then it changes due to the solar irradiance variations. Six cases of DG1 are studied:
(1) Case 1: fixed droop coefficients with virtual impedance $Z_{v,pu}$=0.036+j0.036;
(2) Case 2: enhanced dual-droop control strategy in [4];
(3) Case 3: adaptive droop coefficients with virtual impedance designed by the plug-and-play control rule in [26];
(4) Case 4: the proposed adaptive droop control with adaptive virtual impedance;
(5) Case 5: the proposed method under an unbalanced load condition;
(6) Case 6: comparison between the proposed method and the method in [26] with $\triangle\omega$=0.016 p.u. and $\triangle V$=0.02p.u.

A. *Case 1*

Fig. 8 shows the simulation results of Case 1. As one can find that when S_a is at the rated value, DG1 delivers power (about 5.8kW) proportionally together with other DGs to the loads. The DG1 voltage and system frequency are stable. When S_a decreases to 50% due to solar irradiance variation, the available power of DG1 cannot meet the load demand. Due to the fixed droop coefficients, DG1 keeps outputting power (5.8kW) to the ac side system without being aware of the currently available power of the PV panel. A power imbalance between the dc and ac sides of DG1 occurs. As a result, this power imbalance leads to a collapse of the dc side voltage and a frequency divergence, and subsequently, an unstable system is observed.

B. *Case 2*

When the enhanced dual-droop strategy in [4] is adopted, the results in Fig. 9 show that the strategy is able to ensure system stability when S_a is reduced to 50% with some oscillations in the droop frequency and output voltage of DG1. Due to the decrease of the PV voltage, the dc-link voltage DC droop [4] generates an additional term to reduce the droop frequency, lowering the output active power of DG1. The conventional *P-f* AC droop is now broken and the active power of DG1 is not proportional to its capacity anymore. When S_a is further reduced to 10%, the dc-link voltage droop fails to decrease the output active power effectively, therefore, the PV voltage collapses quickly due to a large power imbalance between the generation and load demand, leading to an unstable system.

C. *Case 3*

In case 3, an active-front-end rectifier load (6.4kW) is connected at N1 in the simulation. According to the plug-and-play rule in [26], a virtual impedance $Z_{v,pu} = (0.03 + j0.03)\, S_N/S_a$ is designed and added based on the adaptive droop scheme. As depicted in Fig. 10, the adaptive droop and virtual impedance

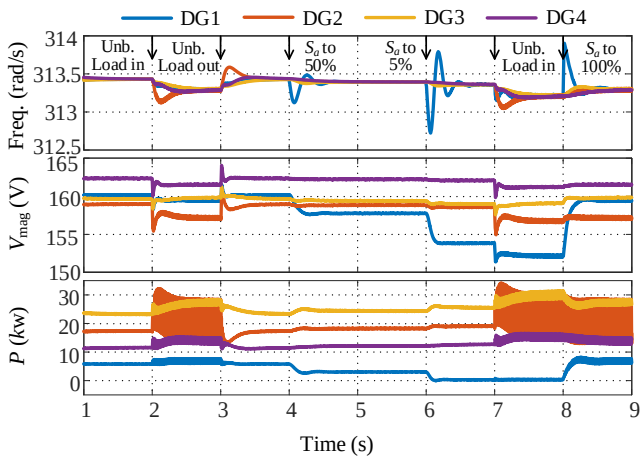

Fig. 12 Simulation results with the proposed adaptive droop and adaptive virtual impedance control under an unbalanced load condition

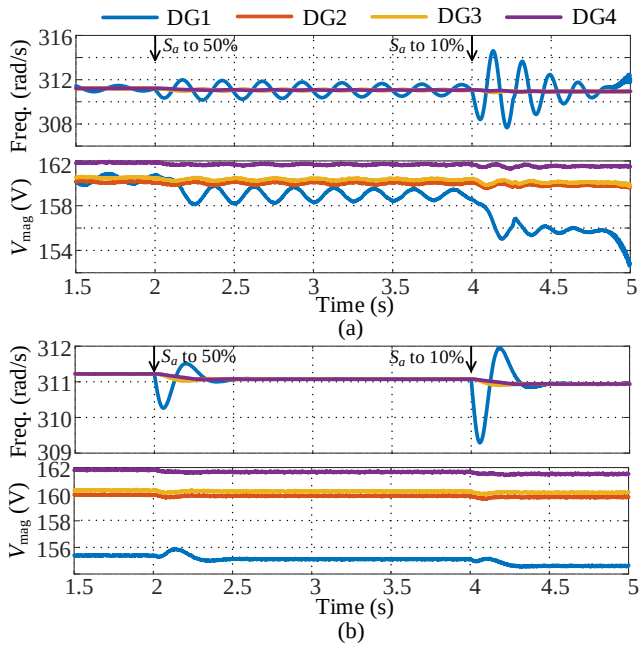

Fig. 13 Simulation results with $\triangle\omega$=0.016 p.u. and $\triangle V$=0.02p.u. (a) the plug-and-play rule in [26]. (b) the proposed designed method

are able to ensure a stable system when S_a varies between 100% and 5%. Since the droop coefficients are altered according to S_a of DG1, the accurate active power-sharing is kept among the DGs.

D. Case 4

With the proposed method and parameters in Table II, the designed adaptive virtual resistance is (23) and the adaptive virtual impedance is (24), which is close to that in case 3. As expected, the results in Fig. 11 are similar to that in Fig. 10. Even there is an active-front-end rectifier load (6.4kW) connecting to N1 at t = 7s, the proposed method can ensure DG1 outputting active power proportionally to its currently available power. Both the results in Fig. 10 and Fig. 11 prove the effectiveness of the adaptive droop and virtual impedance method can handle the uncertainties of S_a and load variations.

E. Case 5

The proposed strategy is also tested under an unbalanced load condition, which is represented by a 3Ω resistor connected between Phase A and C at N2 in the simulation. As shown by the simulation results in Fig. 12, when S_a is the rated power, DG1 picks up some unbalanced load. Since the proposed strategy can only guarantee the averaged power-sharing, the unbalanced load is dispatched automatically according to the negative sequence impedances between the DGs and the load. Hence, DG2 undertakes the majority of the unbalanced load, as indicated by magnitudes of the oscillations in the active powers. When S_a is 5%, the virtual impedance in DG1 has been increased greatly. Therefore, when the unbalanced load is switched in, the unbalanced power of DG1 is reduced. The simulation results verify that the proposed strategy can operate properly under the unbalanced load condition.

F. Case 6

The advantage of the proposed strategy over the method presented in [26] becomes clear under different voltage quality requirements, as shown in Fig. 13. In case 6, the maximum allowed frequency and voltage deviations are changed to $\triangle\omega$=0.016 p.u. and $\triangle V$=0.02p.u. $Z_{v,pu} = (0.03 + j0.03)\,S_N/S_a$ is still applied in [26], while $R_{v,pu}$=$(0.104\,S_N/S_a - 0.012)$ is designed according to (22) in the proposed method. As shown in Fig. 13(a), there are continuous oscillations in the frequency and voltage of DG1. Although the frequency is damping slowly when S_a is reduced to 10%, the oscillations make the output power exceed the generation from the PV and an unstable system is expected. When adopting the proposed virtual impedance, Fig. 13(b) shows that the frequency and voltage can reach a steady-state point quickly when S_a varies because of the large damping effect provided by the virtual impedance.

VI. EXPERIMENTAL RESULTS

The proposed control strategy is further validated based on a laboratory platform with two parallel DGs, as shown in Fig. 14. The inverters are constructed using three-phase two-level CREE MOSFET modules and gate drivers CGD15FB45P1. Two Elektro-Automatik DC sources supply power for the inverters. An OP4510 is used to implement the control algorithms and generate the gate signals for the inverters. The parameters of the platform are listed in Table III. Limited by the power capacities of the dc sources and the rated current of other elements, i.e. filter inductor, an overcurrent protection scheme for the inverter is implemented with a threshold I_{th} = 14A.

First, to reveal the instability problem of the traditional droop under power deficiency, the power of DG1 is limited to represent the power deficiency. The DGs are controlled with constant droop coefficients and a virtual impedance $Z_{v,pu}$=0.036+j0.036 p.u. is used to decouple the active and reactive power droop and to provide system damping. The experimental results are shown in Fig. 15. Initially, the load is shared by the two DGs properly. When the system load increases by 1kW, the power demand exceeds the limitation of the DG1. Consequently, the output power of DG1 decreases while that of DG2 increases, reflecting a diverging system

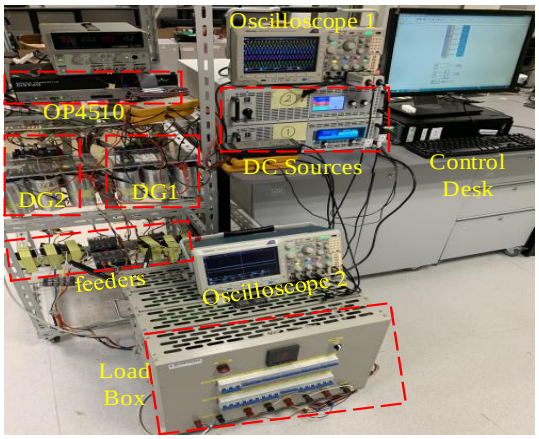

Fig. 14 Experimental Platform

TABLE III PARAMETERS OF DGS IN EXPERIMENTS

Symbol	Description	Values
S_{n1}/ S_{n2}	Rated power of DG1 and DG2	10 kVA/10kVA
E_0	Rated voltage magnitude	165V
ω_0	Rated angular frequency	314.159rad/s
f_s	Switching frequency	21kHz
V_{dc}	DC voltage	400V
f_{ss}	Signal sampling frequency	50kHz
$\triangle\omega$	Allowed frequency deviation	0.2Hz
$\triangle V$	Allowed voltage deviation	8.25V
ω_c	Cutoff frequency of LPF	30rad/s
L_f	Filter inductance	3mH, 0.12Ω
C_f	Filter capacitance	40uF
PR_v	Voltage PR controller	k_{pv}=0.17, k_{rv}=65
PR_c	Current PR controller	k_{pc}=7.3
F	Feedforward gain of output current	0.6
Z_{c1}	Connecting feeder impedance of DG1	0.23Ω, 1.3mH
Z_{c2}	Connecting feeder impedance of DG2	0.15Ω, 0.8mH

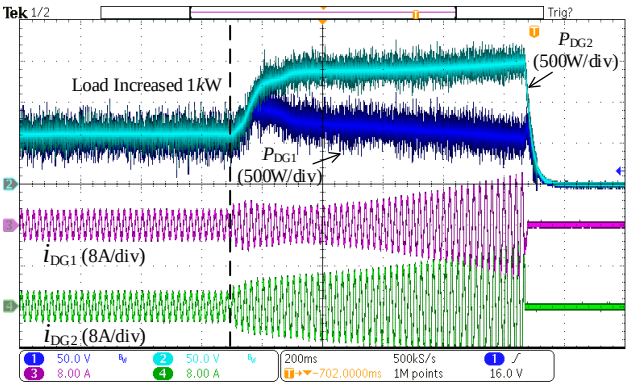

Fig. 15 Experimental results with constant droop coefficients and $Z_{v,pu}$=0.036+j0.036p.u. when DG1 suffers from power deficiency

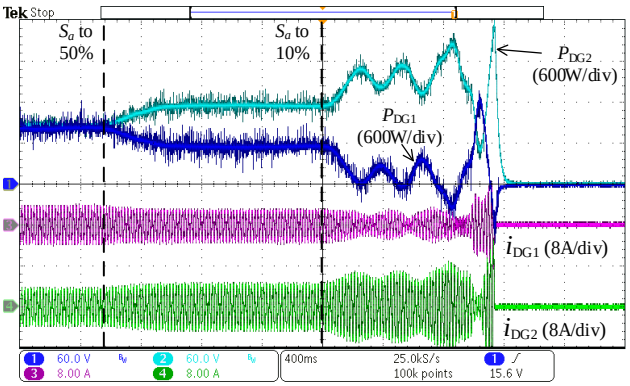

Fig. 16 Experimental results with adaptive droop and constant virtual impedance $Z_{v,pu}$=0.036+j0.036p.u under S_a variations

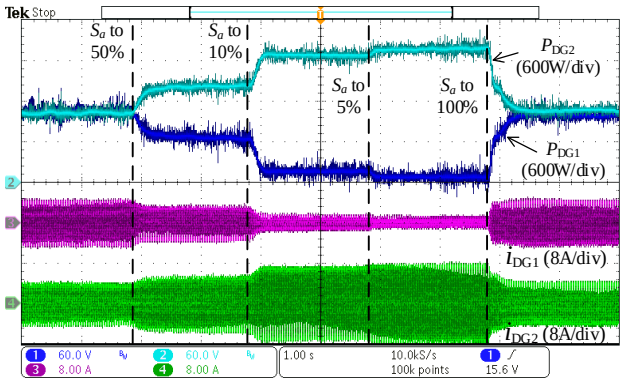

Fig. 17 Experimental results with adaptive droop and the proposed virtual impedance under S_a variations, $\triangle\omega$=0.004 p.u. and $\triangle V$=0.05p.u.

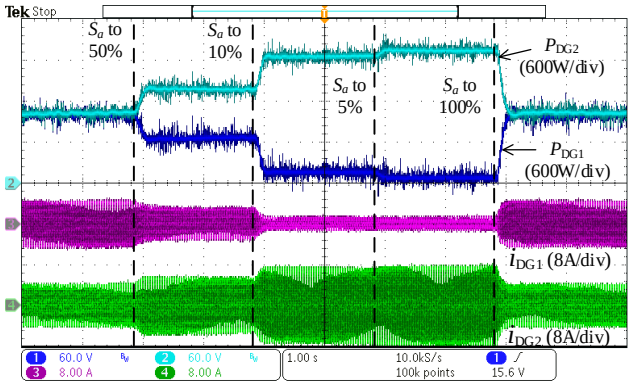

Fig. 18 Experimental results with adaptive droop and the proposed virtual impedance under S_a variations, $\triangle\omega$=0.016 p.u. and $\triangle V$=0.02p.u.

frequency. After a specific time the increasing output currents trigger the overcurrent protection and the DGs are finally tripped. This test shows that conventional droop control cannot continue to achieve proper load sharing and ensure system stability when DGs suffer power deficiency.

When adaptive droop in (2) and constant virtual impedance are adopted, the results are presented in Fig. 16. This case is aimed to prove that, even adaptive droop is applied in respect to DG power variation, system instability may still exist due to the large droop coefficients. As shown in Fig. 16, the two DGs can stably share the load when S_a of DG1 decreases to 50%. However, if S_a drops to 10%, the droop coefficients will be 10 times larger than the original values, which causes increasing oscillations in the output powers and currents. Eventually, the DGs are also tripped for overcurrent.

In the third case, the adaptive virtual impedance designed by (23) and (24) is incorporated into the adaptive droop in (2), Fig. 17 presents the system performance. The common load is comprised of a linear resistive-inductive load (1.2kW, 0.3kVar) and a non-linear load consisting of a dynamic PWM rectifier

(0.8*k*W). It can be seen that when S_a varies between 100% and 5%, the loads are properly shared by the DGs and there are not obvious oscillations in the output powers and currents. This proves that the proposed adaptive virtual impedance droop is able to ensure a stable operation when DG available power varies significantly.

If another set of $\triangle\omega$=0.016 p.u. and $\triangle V$=0.02p.u. is selected, the proposed method adjusts the virtual resistance to $R_{v,pu}$=$(0.104 S_N/S_a - 0.012)$. The experiment results in Fig. 18 are similar to that in Fig. 17, but faster dynamic responses can be observed when S_a varies. The results in Fig. 17 and Fig. 18 together verify that the proposed method can ensure system stability under different $\triangle\omega$ and $\triangle V$.

VII. CONCLUSION

In droop-controlled microgrids with fluctuating outputs from renewable energy resources, it is crucial in achieving a proper and stable load sharing among DGs according to different and varying capacities. In this paper, an adaptive droop and adaptive virtual impedance control strategy is proposed. To avoid the instability caused by the power deficiency of DGs, the droop coefficients are adaptive to the currently available power. After that, an output impedance model of a droop-controlled inverter is developed to analyze the impact of varying droop coefficients on the terminal characteristics of the inverters and the stability of the microgrid system. Then, a novel method is proposed in detail to design an adaptive virtual impedance to counteract the negative influence of large droop coefficients on system stability. The proposed strategy is verified by in-depth analysis, simulation, and experiment. Comparing with several existing methods in the simulation, it can be found that the proposed method has a superior performance under uncertain capacities of DGs and different values of $\triangle\omega$ and $\triangle V$.

APPENDIX

In Fig. 1, a dual-loop inner voltage and current control scheme is used to regulate the output voltage and inductor current. The controllers are implemented in the stationary frame using PR controllers. The output current of the DG is also fed forward with a proportional gain *F*. Therefore, the closed-loop transfer function from the voltage reference to the output voltage is

$$G_v(s) = \frac{G_d(s)PR_c(s)PR_v(s)}{1+G_d(s)G_s(s)\left[PR_c(s)PR_v(s)+Y_{Cf}(s)PR_c(s)-1\right]+Y_{Cf}(s)Z_{Lf}(s)}$$

the closed-loop transfer function from the output current to the output voltage is

$$G_c(s) = \frac{Z_{Lf}(s)+G_d(s)G_s(s)PR_c(s)\left[1-F\right]}{1+G_d(s)G_s(s)\left[PR_c(s)PR_v(s)+Y_{Cf}(s)PR_c(s)-1\right]+Y_{Cf}(s)Z_{Lf}(s)}$$

Here $Z_{Lf}(s)$ is the impedance of the LC filter inductor, $Y_{Cf}(s)$ is the admittance of the LC filter capacitor, $G_d(s)$ is the PWM delay effect, $G_s(s)$ is the voltage and current sampling effect.

REFERENCES

[1] M. Liserre, T. Sauter, and J. Hung, "Future energy systems: integrating renewable energy sources into the smart power grid through industrial electronics," *IEEE Ind. Electron. Mag.*, vol. 4, no. 1, pp. 18-37, Mar. 2010.

[2] Q. Wu, R. Guan, X. Sun, Y. Wang, and X. Li, "SoC balancing strategy for multiple energy storage units with different capacities in islanded microgrids based on droop control," *IEEE JEST Power Electron.*, vol. 6, no. 4, pp. 1932-1941, Jan. 2018.

[3] Y. Shan and et al, "A Model Predictive Power Control Method for PV and Energy Storage Systems with Voltage Support Capability," *IEEE Trans. Smart Grid*, vol. 11, no. 2, pp. 1018-1029, Mar. 2020.

[4] H. P. Liu *et al.*, "An enhanced dual droop control scheme for resilient active power sharing among paralleled two-stage converters," *IEEE Trans. Power Electron.*, vol. 32, no. 8, pp. 6091-6104, Aug. 2017.

[5] X. Chen, L. Wang, H. Sun, and Y. Chen, "Fuzzy logic based adaptive droop control in multiterminal HVDC for wind power integration," *IEEE Trans. Energy Convers.*, vol. 32, no. 3, pp. 1200-1208, Sep. 2017.

[6] J. Hu, Z. Li, J. Zhu, and J. M. Guerrero, "Voltage stabilization: a critical step toward high photovoltaic penetration," *IEEE Ind. Electron. Mag*, vol. 13, no. 2, pp. 17-30, June 2019.

[7] X. Lu, K. Sun, J. M. Guerrero, J. C. Vasquez, and L. Huang, "State-of-charge balance using adaptive droop control for distributed energy storage systems in DC microgrid applications," *IEEE Trans. Ind. Electron.*, vol. 61, no. 6, pp. 2804-2815, Aug. 2014.

[8] K. D. Hoang and H.-H. Lee, "Accurate power sharing with balanced battery state of charge in distributed DC microgrid," *IEEE Trans. Ind. Electron.*, vol. 66, no. 3, pp. 1883-1893, Mar. 2019.

[9] X. F. Sun, Y. C. Hao, Q. F. Wu, X. Q. Guo, and B. C. Wang, "A multifunctional and wireless droop control for distributed energy storage units in islanded AC microgrid applications," *IEEE Trans. Power Electron.*, vol. 32, no. 1, pp. 736-751, Jan. 2017.

[10] W. Du, Q. Jiang, M. J. Erickson, and R. H. Lasseter, "Voltage-source control of PV inverter in a CERTS microgrid," *IEEE Trans. Power Delivery*, vol. 29, no. 4, pp. 1726-1734, Aug. 2014.

[11] J. M. Guerrero, J. C. Vasquez, J. Matas, M. Castilla, and L. G. de Vicuna, "Control strategy for flexible microgrid based on parallel line-interactive UPS systems," *IEEE Trans. Ind. Electron.*, vol. 56, no. 3, pp. 726-736, Mar. 2009.

[12] P. Khayyer and U. Ozguner, "Decentralized control of large-scale storage-based renewable energy systems," *IEEE Trans. Smart Grid*, vol. 5, no. 3, pp. 1300-1307, Apr. 2014.

[13] N. Pogaku, M. Prodanovic, and T. C. Green, "Modeling, analysis and testing of autonomous operation of an inverter-based microgrid," *IEEE Trans. Power Electron.*, vol. 22, no. 2, pp. 613-625, Mar. 2007.

[14] W. Yao, M. Chen, J. Matas, J. M. Guerrero, and Z. M. Qian, "Design and analysis of the droop control method for parallel inverters considering the impact of the complex impedance on the power sharing," *IEEE Trans. Ind. Electron.*, vol. 58, no. 2, pp. 576-588, Feb. 2011.

[15] A. Yogarathinam and N. R. Chaudhuri, "Stability-constrained adaptive droop for power sharing in AC-MTDC grids," *IEEE Trans. Power Syst.*, vol. 34, no. 3, pp. 1955-1965, May 2019.

[16] S. K. Sahoo, A. K. Sinha, and N. K. Kishore "Control techniques in ac, dc, and hybrid ac-dc microgrid: a revew," *IEEE Journal of Emerg. and Selected Topics in Power Electron.*, vol. 6, no. 2, pp. 738-759, Dec. 2018.

[17] L. Guo, S. Zhang, X. Li, Y. W. Li, C. Wang, and Y. Feng, "Stability analysis and damping enhancement based on frequency-dependent virtual impedance for DC microgrids," *IEEE JEST Power Electron.*, vol. 5, no. 1, pp. 338-350, Mar. 2017.

[18] T. Wang, H. Nian, Z. Q. Zhu, L. Ding, and B. Zhou, "Flexible compensation strategy for voltage source converter under unbalanced and harmonic condition based on a hybrid virtual impedance method," *IEEE Trans. Power Electron.*, vol. 33, no. 9, pp. 7656-7673, Sep. 2018.

[19] K. M. Alawasa, Y. A.-R. I. Mohamed, and W. Xu, "Active mitigation of subsynchronous interactions between PWM voltage-source converters and power networks," *IEEE Trans. Power Electron.*, vol. 29, no. 1, pp. 121-134, Jan. 2014.

[20] T. V. Hoang and H. H. Lee, "An adaptive virtual impedance control scheme to eliminate the reactive-power-sharing errors in an islanding meshed microgrid," *IEEE JEST Power Electron.*, vol. 6, no. 2, pp. 966-976, Jun. 2018.

[21] H. Mahmood, D. Michaelson, and J. Jiang, "Accurate reactive power sharing in an islanded microgrid using adaptive virtual impedances," *IEEE Trans. Power Electron.*, vol. 30, no. 3, pp. 1605-1617, Mar. 2015.

[22] B. Liu, Z. Liu, J. Liu, R. An, H. Zheng, and Y. Shi, "An adaptive virtual impedance control scheme based on small-AC-signal injection for unbalanced and harmonic power sharing in islanded microgrids," *IEEE Trans. Power Electron.*, pp. 1-1, Dec. 2019.

[23] J. Zhou, S. Kim, H. Zhang, Q. Sun, and R. Han, "Consensus-based distributed control for accurate reactive, harmonic, and imbalance power sharing in microgrids," *IEEE Trans. Smart Grid*, vol. 9, no. 4, pp. 2453-2467, Jul. 2018.

[24] Y. Hu, Y. Shao, R. Yang, X. Long, and G. Chen, "A configurable virtual impedance method for grid-connected virtual synchronous generator to improve the quality of output current," *IEEE JEST Power Electron.*, pp. 1-1, May 2019.

[25] X. Y. Wu, C. Shen, and R. Iravani, "Feasible range and optimal value of the virtual impedance for droop-based control of microgrids," *IEEE Trans. Smart Grid*, vol. 8, no. 3, pp. 1242-1251, May 2017.

[26] P.-H. Huang, P. Vorobev, M. Al Hosani, J. L. Kirtley, and K. Turitsyn, "Plug-and-play compliant control for inverter-based microgrids," *IEEE Trans. Power Syst.*, vol. 34, no. 4, pp. 2901-2913, Jul. 2019.

[27] M. Dokus and A. Mertens, "Sequence impedance-based stability analysis of droop-controlled AC microgrids," in *2019 IEEE 10th International Symposium on Power Electronics for Distributed Generation Systems (PEDG)*, 2019: IEEE, pp. 768-773,

[28] J. M. Guerrero, L. G. de Vicuna, J. Matas, M. Castilla, and J. Miret, "Output impendance design of parallel-connected UPS inverters with wireless load-sharing control," *IEEE Trans. Ind. Electron.*, vol. 52, no. 4, pp. 1126-1135, Aug. 2005.

[29] Y. Shan, J. Hu, M. Liu, J. Zhu, and J. M .Guerrero, "Model Predictive Voltage and Power Control of Islanded PV-Battery Microgrids with Washout Filter Based Power Sharing Strategy," *IEEE Trans. Power Electron.*, vol. 35, no. 2, pp. 1227-1238, Feb. 2020.

[30] D. M. Pham and H.-H. Lee, "Effective coordinated virtual impedance control for accurate power sharing in islanded microgrid," *IEEE Trans. Ind. Electron.*, pp. 1-1, Feb. 2020.

ZilinLi (S'17) received the B.Sc. degree in electrical engineering from China Agricultural University, Beijing, China, in 2011, and the M.Sc. degree in electrical engineering from South China University of Technology, Guangzhou, China, in 2017. He is currently working toward the Ph.D. degree in electrical engineering at The Hong Kong Polytechnic University, Hong Kong. His research interests include power electronics and microgrids.

Ka Wing Chan (M'98) received the B.Sc. (Hons) and Ph.D. degrees in electronic and electrical engineering from the University of Bath, U.K., in 1988 and 1992, respectively. He currently is an Associate Professor and Associate Head in the Department of Electrical Engineering of the Hong Kong Polytechnic University. His general research interests include power system stability, analysis and control, power grid integration, security, resilience and optimization, demand response management, etc.

Jiefeng Hu (S'12–M'14–SM'16) received the Ph.D. degree in electrical engineering from University of Technology Sydney (UTS), Australia, in 2013. He parpiciated in the research of minigrids in Commonwealth Scientific and Industrial Research Organization (CSIRO), Newcastle, Australia. He was an Assistant Professor at The Hong Kong Polytechnic University, Hong Kong. Currently he is an Associate Professor and Program Coordinator of Electrical and Information Engineering at Federation University Australia. His research interests include power electronics, renewable energy, and smart microgrids. He received the Best Paper Award in IET International Conference on Advanced Power System Control, Operation and Management (APSCOM) 2018. He is an Associate Editor of IET Renewable Power Generation, an Editor of IEEE Transactions on Energy Conversion, and a Guest Editor of IEEE Transactions on Industrial Electronics.

Josep M. Guerrero (S'01-M'04-SM'08-FM'15) received the B.S. degree in telecommunications engineering, the M.S. degree in electronics engineering, and the Ph.D. degree in power electronics from the Technical University of Catalonia, Barcelona, in 1997, 2000 and 2003, respectively. Since 2011, he has been a Full Professor with the Department of Energy Technology, Aalborg University, Denmark, where he is responsible for the Microgrid Research Program (www.microgrids.et.aau.dk). His research interests is oriented to different microgrid aspects, including power electronics, distributed energy-storage systems, hierarchical and cooperative control, energy management systems, smart metering and the internet of things for AC/DC microgrid clusters and islanded minigrids; recently specially focused on maritime microgrids for electrical ships, vessels, ferries and seaports. Prof. Guerrero is an Associate Editor for a number of IEEE TRANSACTIONS. He received the best paper award of the IEEE Transactions on Energy Conversion for the period 2014-2015, and the best paper prize of IEEE-PES in 2015. In 2015 he was elevated as IEEE Fellow for his contributions on "distributed power systems and microgrids."